Half-Mirror for Electrons in Quantum Hall Copropagating Edge Channels in a Mach-Zehnder Interferometer

Takase Shimizu,[1,*] Jun-ichiro Ohe,[2] Akira Endo,[1] Taketomo Nakamura,[1] and Shingo Katsumoto[1]

[1] *Institute for Solid State Physics, The University of Tokyo, 5-1-5 Kashiwanoha, Kashiwa, Chiba 277-8581, Japan*

[2] *Department of Physics, Toho University, 2-2-1 Miyama, Funabashi, Chiba 274-8510, Japan*

(Received 14 September 2022; revised 10 January 2023; accepted 23 February 2023; published 27 March 2023)

A half-mirror that divides a spin-polarized electron into two parallel copropagating spin-resolved quantum Hall edge channels one half each is presented in this study. The partition process is coherent, as confirmed by observing the Aharonov-Bohm oscillation at high visibility of up to 85% in a Mach-Zehnder interferometer, which comprises two such half-mirrors. The coherence length of the interferometer exceeds 200 μm, which reflects the robust nature of the copropagating channels against the decoherence caused by the coupling to the environment. In addition, the device characteristics are highly stable, making the device promising in the application of quantum information processing. The beam-splitting process is theoretically modeled, and the numerical simulation successfully reproduces the experimental observation. The partition of the electron accompanied by the spin rotation is explained by the angular momentum transfer from the orbital to the spin via spin-orbit interactions.

DOI: 10.1103/PhysRevApplied.19.034085

I. INTRODUCTION

Owing to their chiral nature, quantum Hall edge channels (QHECs) present a significantly high quantum coherence, as evidenced by the operations of the Mach-Zehnder interferometers (MZIs) [1], and Fabry-Perot interferometers [2,3], which both revealed fractional statistics of quasiparticles. The high quantum coherence in QHECs has expanded the field of "electron quantum optics," in which the one-dimensional edge states work as quantum beams. These quantum beams have gained attention not only from physicists as fermionic beams with many-body interactions [4], but also from researchers relative to quantum information processing [5]. Considering the latter, the electron quantum optical circuits have twofold roles: being the carrier of quantum information, "wiring" clusters of qubits, and processing the quantum information within themselves [6]. Here, we focus on the latter, where quantum gate operations are required on the beams of the circuits. Several experimental and theoretical efforts have been made to construct building blocks of quantum circuits with QHECs [7,8], such as single-electron sources [9–12], detectors [13], and controlled phase shifters [14]. These electron quantum beams have an orbital (charge) degree of freedom and a spin degree of freedom. When the spin-orbit interaction (SOI) is weak, two paths with quantum tunneling should be prepared for the orbital operation [5], whereas a single path is sufficient for the spin, which is the internal degree of freedom [15,16]. In both ways, each electron traveling on the track of the beams can be viewed as a flying qubit (FQ), which carries the quantum information of one qubit.

Half-mirrors or beam splitters (BSs) with a 1:1 ratio [17] are essential for quantum optical operations. As electrical BSs, quantum point contacts (QPCs), which partially transmit electrons and reflect the residual part to a *counterpropagating* QHEC, have been utilized in most experiments performed thus far [18]. This property stems from the chiral nature of QHECs that sustains the coherence and is unavoidable for the QPC BS scheme [19]. The transition probability is controllable with a gate voltage of up to 50%, at which the QPC functions as a Hadamard gate [20,21].

Although the QPC-BS scheme has several advantages, e.g., controllability, it presents certain drawbacks. For instance, the area occupied by the MZI becomes inevitably large since the counterpropagating nature of the split beams requires a Corbino-type structure. Generally, the scalability of the solid-state circuit is a crucial advantage over the optical quantum circuit. However, the large-area consumption in the QPC-BS scheme largely reduces the scalability. Furthermore, the area consumption also leads to instability in quantum gate operations because the Aharonov-Bohm (AB) phase, a critical parameter in the qubit operation, fluctuates with the fluctuation of the external field and the gate voltages determining the area [1]. Another problem related to the instability is a type

*takase.shimizu@ntt.com

of crosstalk; that is, the QPC partition ratio tends to be affected by the surrounding gate operations of the qubits. The QPC should function in a transition region between conductance plateaus, where the ratio is sensitive to the small electric fields, as indicated by its application to single-charge sensors [22]. We also highlight that the freedom in designing quantum circuits with QPC BSs is limited due to topological constraints, such as the complex series concatenation of MZIs.

The BS device described in this study functions between *copropagating* spin-split QHECs. The spin splitting of QHECs is caused by the Zeeman effect enhanced by the exchange of coupling between the electron spins, which lines up the spins in parallel inside the channels. The series connection of multiple quantum gates is available [23], thus providing extensive freedom in the circuit design. The distances between spin-split QHECs are generally short, and the circuit areas can be reduced by decreasing the distances between consecutive BSs, thus enhancing the stability of circuits. Here, a beam-splitting action, such as partial interchannel tunneling, is a challenge that should be associated with spin flipping. Previous studies regarding this type of tunneling transition used current imbalance [24–26], and periodic magnetic gates with up to 28% of transition probability [27,28]. Nakajima *et al.* [29,30] reported that spin flips occurred at corners of the QHECs because the effective magnetic field of a spin-orbit interaction [31] changes nonadiabatically. We also recently reported spin flips at corners: the transition probability can be controlled by modulating the curvature of the QHECs by controlling the electrostatic potential via gate voltages [32]. However, the estimated transition probability of the BS was only up to 2%, which is significantly below 50% (half-mirror condition). Thus, the aforementioned absolute criterion of quantum information processing was not fulfilled. Considering the geometrical effects [33,34] and spin-rotation mechanism [32], a higher transition probability should be obtained by sharpening the corner, that is, enhancing the curvature.

This study presents a half-mirror for copropagating spin-split QHECs with an acute-angle gate, which gains a high probability in nonadiabatic transition via SOI. The transition probability can be controlled from 0% to above 50% with gate voltages by modulating the spatial distance between the channels at the bending point. A high quantum coherence over the transition is confirmed by observing the AB interference in the MZI composed of two series BSs.

II. EXPERIMENTAL METHODS AND RESULTS

Method.–Figure 1(a) presents a schematic of the BS device fabricated on a two-dimensional electron system (2DES) in the spin-split integer quantum Hall regime. The device consists of three Schottky gates: gate G_a is for beam splitting, and gates SF_b and SF_c are for spin filtering. The external circuits and QHECs are illustrated in the figure. Only QHECs with the spin-resolved Landau indices of $j = 1$ and 2 are depicted in the figure, although the filling factor $\nu = 4$ in the nongated region is used in this experiment. The channels with $j = 3$ and 4 lying in the interior of the 2DES are omitted for simplicity. We focus on the two QHECs, denoted as channel 1 (red) and channel 2 (blue), in which spins are locked at $\uparrow$ and $\downarrow$, respectively. Beneath the spin-filter gates denoted as SF_b and SF_c, the filling factors ν_b and ν_c are tuned to 1 so that only channel 1 proceeds through them [35,36]. Gate G_a is tuned to deplete the electrons under the gate. In this configuration, an electron injected into channel 1 from the right electrode at the bias voltage V_{ac} meets channel 2 at the left corner of gate SF_b, and propagates to the right corner of gate SF_c. The partial transition from channel 1 to 2 occurs through a local SOI [32] as a result of the orbits wrapping around the sharp corner of gate G_a, annotated as "Splitting point." The transition ratio is detected as the ratio of the currents through the left and bottom contacts, $I_\uparrow$ and $I_\downarrow$, respectively. Based on the Landauer-Büttiker formula [19], the transition probability at the BS to channel 2 is given by $\mathcal{T}_\downarrow = G_\downarrow/(e^2/h)$, where $G_\downarrow \equiv dI_\downarrow/dV_{ac}$ is the differential conductance, and e^2/h is the quantized conductance with an electron charge $-e$ and Planck constant h.

A two-dimensional electron system (2DES) with an electron density of 3.8×10^{11} cm^{-2} and a mobility of 90 m^2/Vs in a $Al_xGa_{1-x}As/GaAs$ ($x = 0.265$) single heterostructure is used as a base system for the sample. The structure of the wafer (from the front surface) consists of a 5-nm Si-doped GaAs cap layer, 40-nm Si-doped ($N_{Si} = 2 \times 10^{18}$ cm^{-3}) $Al_xGa_{1-x}As$ layer, 15-nm undoped $Al_xGa_{1-x}As$ spacer layer, and an 800 nm GaAs layer with a 2DES residing near the interface with the upper layer. Figure 1(b) presents an optical micrograph of the sample with the configuration of the Au/Ti gates and ohmic contacts. Three devices, including the beam splitter, interferometer, and control device, are fabricated on a single substrate. The magnified views (from a scanning electron micrograph) of the beam splitter and the MZI are shown in Figs. 1(c) and 1(d), respectively. The crystal orientation depicted in Fig. 1 is chosen to enlarge the rotation angle of the sum of the effective fields of the Rashba and Dresselhaus SOI at the corner [37].

We cool the sample down to 35 mK (except for the measurements in Fig. 6) and apply a perpendicular magnetic field B up to 8 T, at which the 2DES is in the quantum Hall state with a filling factor of $\nu = 2$. We measure the differential conductances $G_{\uparrow,\downarrow} \equiv dI_{\uparrow,\downarrow}/dV_{ac}$ using the standard lock-in technique with a small modulation voltage 25 μV_{rms} (except for the measurements in Fig. 4) with the frequency 170 Hz. We first measure the gate-voltage dependence of the two-terminal conductance of the spin-filter gates $SF_{b,c,d,e}$ at several magnetic fields, as provided in the Supplemental Material [38]. The gate

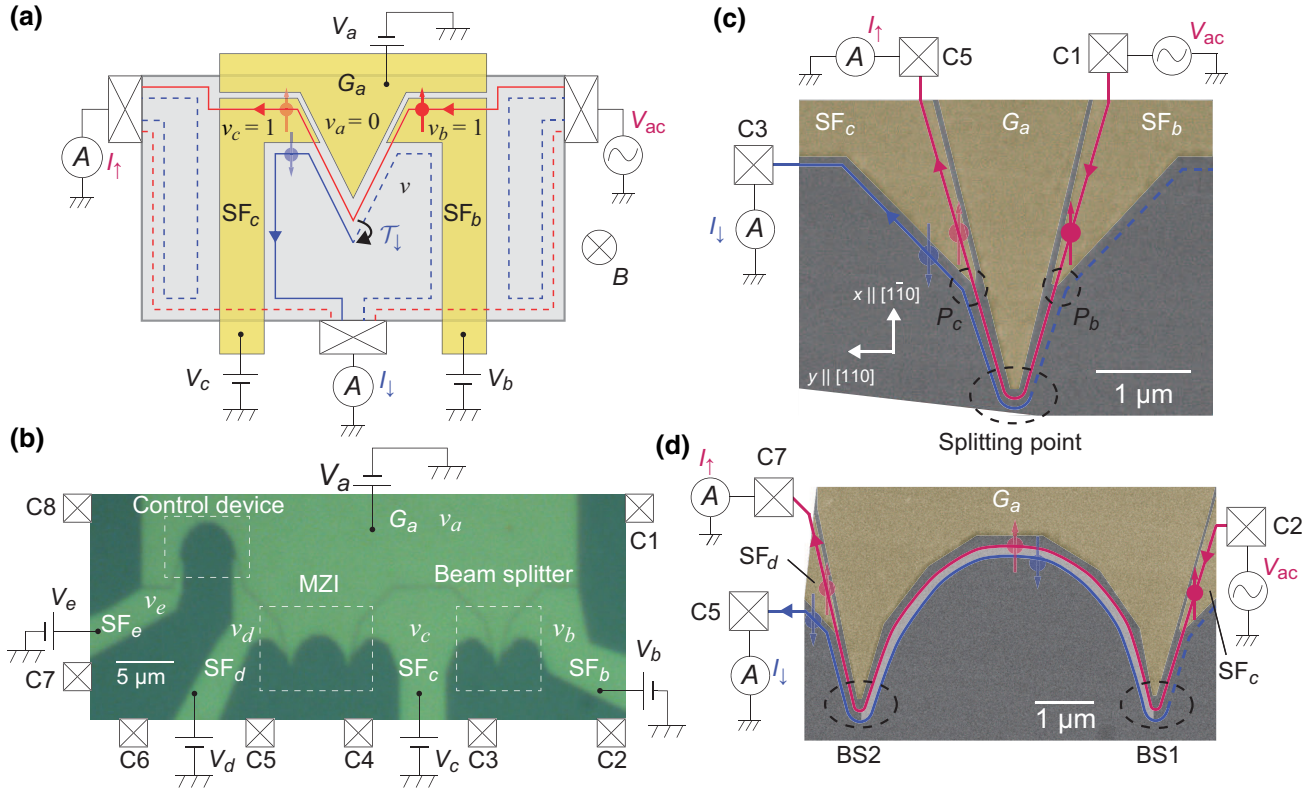

FIG. 1. (a) Schematic of the BS device. Channels 1 and 2 are indicated by the red and blue lines, respectively. (b) Optical micrograph of the sample with the gate and Ohmic contact configuration. Brighter regions indicate the five metallic gates annotated as gate G_a and spin-filter gates SF$_{b,c,d,e}$. Filling factors under the gates are annotated as $\nu_{a,b,c,d,e}$. (c) Magnified view of the BS obtained by a scanning electron microscope (gates are yellow). The parameters are set to $\nu_a = \nu_d = 0$ and $\nu_b = \nu_c = 1$. For the measurement of $\mathcal{T}_\downarrow$, $V_{\rm ac}$ is applied to contact C1, and the currents at contact C5 and C3 are measured as $I_\uparrow$ and $I_\downarrow$, respectively. (d) Magnified view of the MZI. The settings for the interferometry are $\nu_c = \nu_d = 1$, $\nu_b = \nu_e = 0$; V_a is applied in the range of $\nu_a = 0$. For the measurement of the interference, $V_{\rm ac}$ is applied to contact C2, and the current at contacts C7 and C5 are measured as $I_\uparrow$ and $I_\downarrow$, respectively.

voltages for the spin filters are set around the centers of e^2/h plateaus.

Beam splitter.—The experimental results of the BS device are presented herein. As illustrated in Fig. 1(a), we first set $\nu_b = \nu_c = 1$ by applying $V_b = V_c = -0.28$ V. Then, we changed V_a from 0.1 V to −1 V. Figure 2(a) demonstrates the V_a dependence of $G_{\uparrow,\downarrow}$ at $B = 4.1$ T ($\nu = 3.8$). The inset in Fig. 2(a) presents the data in the region from $V_a = 0.1$ V to −0.3 V, where four plateaus corresponding to $\nu_a = 4, 3, 2, 1$ are observed. This manifests that there are two extra QHECs inside the 2DES, other than channels 1 and 2, as shown in Fig. 1(a). However, the tunneling rate from channels 1 and 2 to the extra QHECs is significantly low (less than 2%, as indicated within the Supplemental Material [38]), thus the two additional channels are ignored in subsequent discussions. When V_a is driven to be more negative than approximately equal to −0.4 V, $G_\uparrow$ starts to decrease from e^2/h and $G_\downarrow$ increases by the same amount. This indicates the division of the current into channels 1 and 2. At $V_a \approx -0.85$ V, $\mathcal{T}_\downarrow$ reached 50%, and $\mathcal{T}_\downarrow$ demonstrated an oscillatory behavior by further decreasing V_a. Because this critical value (−0.5 V) of V_a is near the voltage that corresponds to the establishment of the acute angle paths of channels 1 and 2 as shown below, the behavior in Fig. 2(a) indicates that the transmission is mostly around the acute angle, referred to as the "Splitting point" (SP) in Fig. 1(c).

The behavior mentioned above of $\mathcal{T}_\downarrow$ for V_a can be explained by considering the V_a dependence of the distance between channels 1 and 2 around the SP. A numerical calculation using the finite-element method demonstrates that the equipotential lines around gate G_a intricately change against V_a, as shown in Fig. 3. Based on the two-terminal conductance of the spin filters, most of the 2DES below gate G_a is determined to be depleted at $V_a \approx -0.35$ V, and channel 1 approaches channel 2. Nevertheless, $G_\downarrow$ remains zero in this region because $V_a = -0.35$ V is insufficient to deplete electrons below the splitting point of G_a owing to the narrow shape of the gate; thus, channels 1 and 2 remain spatially separated at the splitting point, as

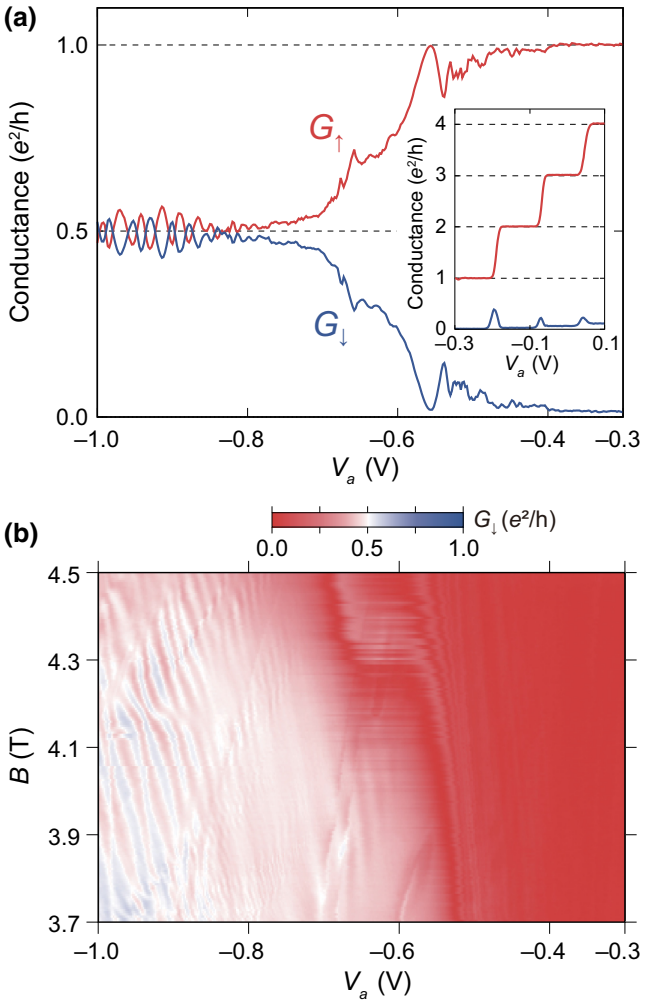

FIG. 2. Outputs of the beam splitter. The data are obtained in the configuration shown in Fig. 1(c) with $V_b = V_c = -0.28$ V ($\nu_b = \nu_c = 1$) and $V_d = -0.5$ V ($\nu_d = 0$). (a) V_a dependence of $G_{\uparrow,\downarrow}$ at $B = 4.1$ T ($\nu = 3.8$). The inset presents the data from $V_a = 0.1$ V to -0.3 V. (b) Color plot of $G_\downarrow$ as a function of V_a and B.

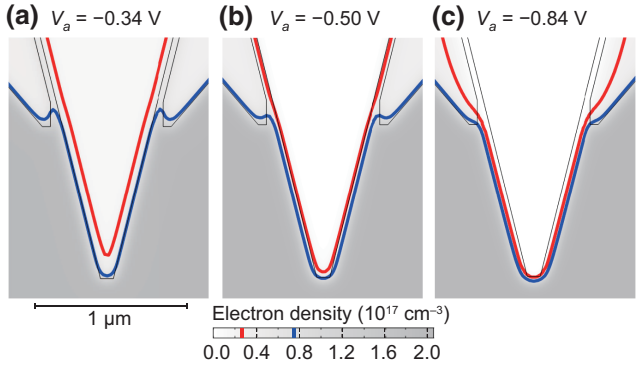

FIG. 3. A grayscale plot of the electron density N at a depth of 64 nm from the surface, which is calculated with the finite-element method described within the Supplemental Material [38] for various center gate voltages V_a. The equipotential lines of $(1/2)(N_0/\nu)$ and $(3/2)(N_0/\nu)$, where $\nu = 4$ and N_0 are the electron densities in the nongated region, are plotted in red and blue, indicating the position of channels 1 and 2, respectively. The voltage of the spin filters is set to -0.28 V in this simulation, which is the same as that in the experiment. (a) Plot of $V_a = -0.34$ V. (b) Plot of $V_a = -0.5$ V. (c) Plot of $V_a = -0.84$ V.

shown in Fig. 3(a). $G_\downarrow$ began to increase with a negative V_a at approximately -0.5 V, where the 2DES at the SP starts to deplete, further leading channel 1 to approach channel 2 and thus enhancing the transition rate.

Figure 2(b) presents a color plot of $G_\downarrow$ on the plane of V_a and B in the $\nu = 4$ plateau region. The overall trend is that $G_\downarrow$, hence $\mathcal{T}_\downarrow$ decreases with an increase of B, reflecting an increase in the distance between channels 1 and 2 at the SP [32]. The weak oscillation of $G_{\uparrow,\downarrow}$ in the region $V_a < -0.85$ V slowly shifts with B, indicating that this is owing to an AB interference with a significantly narrow area of the interference loop. As shown in Fig. 1(c), in addition to the SP, the beam splitter has two bending points of channels 1 and 2 at the vertices of SF_b and SF_c, noted as P_b and P_c, respectively. These two points may function as extra nodes of the electron beams and form weak interferometers combined with the SP. As shown within the Supplemental Material [38], the starting point of the oscillation in V_a shifted with V_b, while it is insensitive to V_c, indicating that P_b functions as a weak node and P_c does not, although no clear explanation for the difference can currently be provided.

Mach-Zehnder interferometer.—Observing the interference is a direct way to test the quantum coherence over the beam-splitting process. For the experiment of the MZI configuration displayed in Fig. 1(d), we first set $\nu_c = \nu_d = 1$ and $\nu_b = \nu_e = 0$ for the two channels under consideration to run as illustrated. The following is obtained from the Landauer-Büttiker formula: $\mathcal{T}_\downarrow = |r_1 e^{i\phi_1} t_2 + t_1 e^{i\phi_2} r_2|^2 = |t_1 r_2|^2 + |r_1 t_2|^2 - 2|t_1 t_2 r_1 r_2| \cos\phi$. Here, t_i (r_i) is the transmission (reflection) amplitude of the ith BS fulfilling $|r_i|^2 + |t_i|^2 = 1$, and [29,32]

$$\phi = \phi_1 - \phi_2 = 2\pi \frac{wLB}{h/e} \tag{1}$$

is the AB phase, where w is the width of incompressible strip [39,40] between channels 1 and 2 averaged over the arclike curve, and L is the length of the arclike curve. The visibility of the oscillation is defined as $\mathcal{V} \equiv (\mathcal{T}_{\downarrow\max} - \mathcal{T}_{\downarrow\min})/(\mathcal{T}_{\downarrow\max} + \mathcal{T}_{\downarrow\min})$, where $\mathcal{T}_{\downarrow\max\,(\min)}$ is the maximum (minimum) value of the oscillation of $\mathcal{T}_\downarrow$.

Figure 4(a) presents the B dependence of $G_\downarrow$ at $V_a = -0.75$ V, where the single BS in Fig. 1(c) has a 50% transition rate. Because the two vertices in Fig. 1(d) have the same angle as that in Fig. 1(c), we can expect that in $\mathcal{T}_{1,2} \equiv |t_{1,2}|^2 \approx 0.5$. $G_\downarrow$ oscillates as a function of B, with

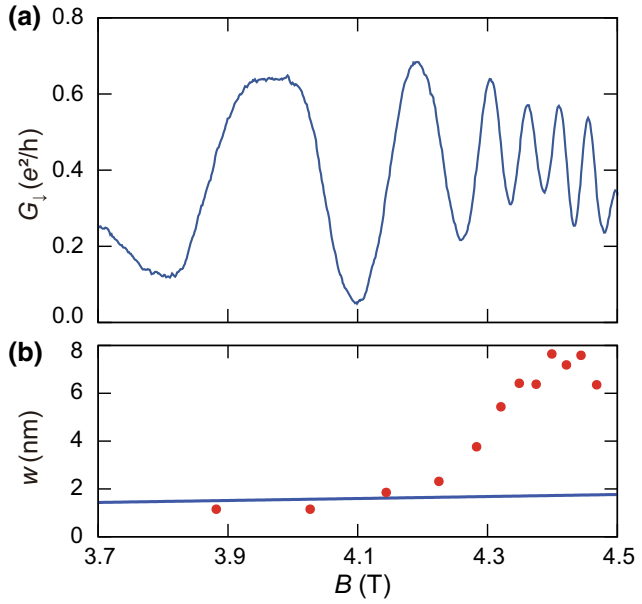

FIG. 4. (a) $G_\downarrow$-output of the MZI device on $\nu = 4$ plateau as a function of B. The gate voltages are set to achieve the channels, as illustrated in Fig. 1(d). V_a on G_a is fixed to -0.75 V. $V_{ac} = 10\ \mu V_{rms}$. (b) Red dots indicate the width of the incompressible strip w obtained from the oscillation data as $w = (2/3)(h/e)/L\Delta B$ at $V_a = -0.75$ V, where ΔB is estimated to be twice the distance between the adjacent oscillation peak and dip, and $L = 8.28\ \mu$m. The blue line indicates w calculated from Eq. (2) with the following parameters: $g^* = -0.6$ [32]; $\epsilon = 12.35$ [41].

a significantly high visibility of $\mathcal{V} \approx 85\%$ at $B \approx 4$ T (see also Fig. 6). $\mathcal{V}$ decreases above 4.1 T, which is probably due to the shifts of $\mathcal{T}_{1,2}$ from the optimal condition.

The oscillation period significantly decreases above 4.2 T, which can be explained in the same manner as in Ref. [32]. In a classical electrostatic model of the QHECs [39, 40], w is given by

$$w \approx \sqrt{\frac{8|g^*\mu_B B|\epsilon\epsilon_0}{\pi e^2 (dn/dr)|_{r=r'}}}, \tag{2}$$

where r' is the center position of the incompressible liquid strip between channels 1 and 2 from the edge of gate G_a; $\epsilon\epsilon_0$ is the dielectric permittivity of the matrix semiconductor; $n(r)$ is the electron sheet density profile, and $g^*\mu_B B$ is the exchange-aided Zeeman splitting, where g^* is the effective Landé g factor; and μ_B is the Bohr magneton. In Fig. 4(b), the red dots indicate the values of w that are experimentally estimated using equation $w = (2/3)(h/e)/L\Delta B$, where ΔB is the oscillation period in B (see Ref. [32] for the detail). The blue line indicates the value of w calculated using Eq. (2), with which the estimated w reasonably agrees below 4.2 T, though it starts to deviate above that. The deviation most likely arises from the breakdown of our assumption $w \propto \sqrt{B}$ above 4.2 T. The exchange interaction is demonstrated to lead to a stronger B dependence of w [42–44]. Furthermore, $B \approx 4.2$ T is the field where the edge state transforms from a spin-textured state to a spin-polarized state [45–48], and the exchange enhancement should be enlarged [49].

Figure 5 presents a color plot of $G_\downarrow$ as a function of V_a and B. The oscillation pattern appears as curved stripes below $V_a \approx -0.6$ V. This arclike pattern is also observed in a previous study [32] and successfully explained with the electrostatic treatment of QHECs [39,40], which reveals that w initially decreases with decreasing V_a but then shows upturn below a certain voltage determined by the depth of the 2DES from the surface ($V_a \approx -0.65$ V for the 2DES used in the present study) [50]. The apparent AB oscillation proves that the transition at the BS is highly coherent, eliminating the possibilities of other transition processes, that is, charge equilibration via impurity scattering [51–53]. Note, the visibility of 85% indicates only the lower boundary of coherence. For the configuration of MZI in this study, the fine and independent tuning of the partition rates of the BSs is not possible, and it may have prevented the BS conditions from being tuned to the optimal point. Although the BS is highly coherent, the results in the control device (SM, VI) indicate that a certain amount of dephasing is caused by the interchannel transition on the gate-defined curve. We note that the obtained values of w [1–8 nm, see Fig. 4(b)] are shorter than the magnetic length ($l_B = 11$ nm at $B = 5$ T). Thus, there must be a significant spatial overlap between the wave functions hence the charge distributions of the two channels. Noting, however, that the interference results from the difference in the AB phase between the states propagating along the two channels and that the "states" are represented by the locations of the guiding center, the overlapping does not diminish the visibility of the interference so long as the intermixing of the spin states by spin-flip scatterings is negligibly small. To minimize the spin-flip by the SOI, the curvature of the channels should be kept as small as possible.

To obtain quantitative information on the coherence of the MZI, we measure the temperature dependence of the visibilities presented in Fig. 6(a). The visibilities monotonically decrease with temperature, revealing the decrease of coherence length l_φ. Except for the temperature below approximately equal to 300 mK and below approximately equal to 4.3 T, the visibilities decay exponentially with temperature. In this exponential decay region, l_φ is deduced from [54,55]

$$\mathcal{V} = \mathcal{V}_0 \exp(-T/T_0) = \mathcal{V}_0 \exp(-2L/l_\varphi), \tag{3}$$

where T_0 is the characteristic temperature inversely proportional to the arm length L, and $\mathcal{V}_0$ is the temperature-independent part of the visibility. Figure 6(b) presents l_φ

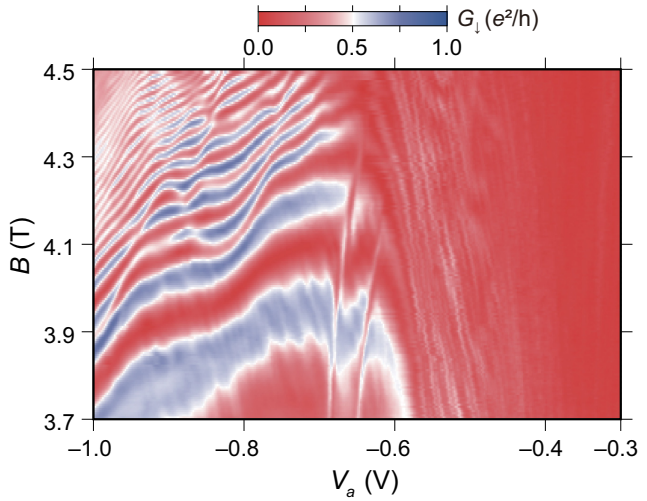

FIG. 5. Color plot of measured $G_\downarrow$ as a function of V_a and B obtained for the MZI.

at $T = 20$ mK (the temperature chosen for the comparison with Ref. [54]) obtained by the exponential fitting on the visibilities and from the relation $l_\varphi = 2LT_0/T$ [54] (for $B < 4.3$ T, we perform the fitting within the exponential decay region above 300 mK). Remarkably, the coherence length exceeds 200 μm, which is an order of magnitude longer than that obtained in the previous MZI using counterpropagating QHECs [54].

We believe that the spatial closeness of the interference paths is the origin of such robustness in coherence. The decoherence in the exponential decay region is attributed to the thermal noise in the surrounding QHECs, which is capacitively coupled to the MZI arms [56]. In our MZI, the MZI arm (spin-resolved Landau indices of $j = 2$) and surrounding QHEC ($j = 3$) are separated by the cyclotron gap, so the spatial separation is larger than that in the previous MZI separated by the Zeeman gap. Thus, our MZI using copropagating QHEC has intrinsically small capacitive coupling to the surrounding QHECs and does not require additional gates for the isolation [57,58]. On the other hand, the two interference paths are very close, resulting in a much larger capacitive coupling between them. Particularly the second point makes a significant difference in the decoherence from the MZIs with large separation in the interference paths because, in the present case, it is very hard for the electromagnetic environment to affect the two paths *differently* [59]. In other words, even if some external noise causes a phase shift in one of the paths, the other gets almost the same phase shift, resulting in the survival of the coherence.

Below $B \approx 4.3$ T, apparent saturation of the visibility is observed below $T \approx 300$ mK. It is unlikely that the saturation is caused by the electron heating because the exponential decay is observed down to the lower temperature in $B > 4.3$ T. The visibility saturation has also

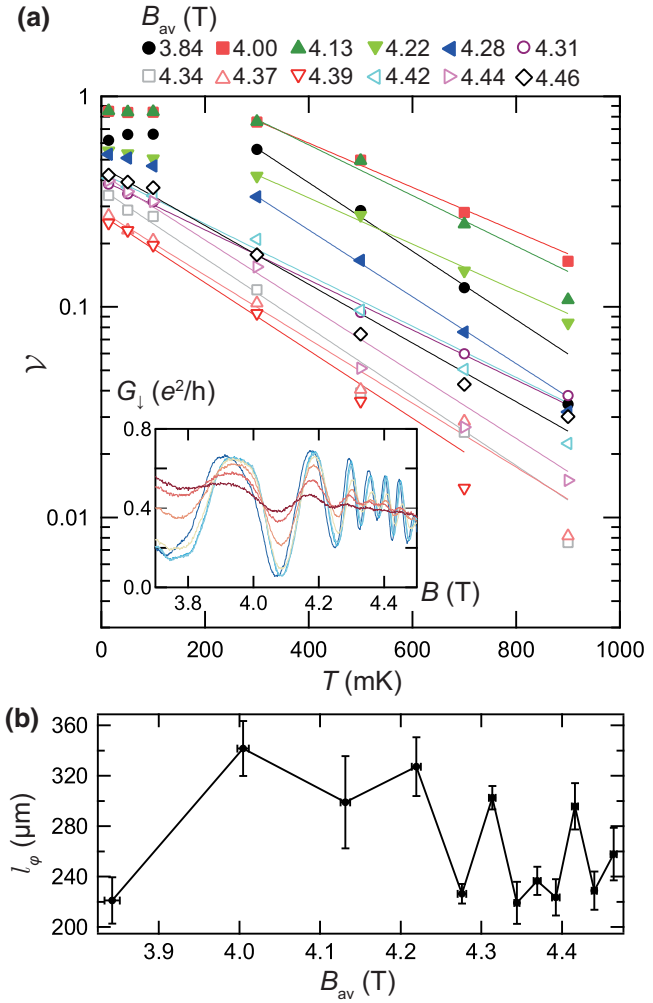

FIG. 6. (a) Temperature dependence of the visibility $\mathcal{V}$ at various magnetic fields B_{av} indicated in the figure. The inset shows the original traces of $G_\downarrow$ versus B taken at various temperatures T ranging from 14 mK to 900 mK. V_a is fixed to −0.75 V. $\mathcal{V}$ is extracted from the adjacent oscillation peak and dip and B_{av} is the center field between them. (b) Coherence length l_φ deduced from the relation $l_\varphi = 2LT_0/T$ [54] at $T = 20$ mK, where T_0 is extracted from the exponential fits according to Eq. (3).

been reported in graphene [60,61] as well as in GaAs [55,62], and Ref. [60] reported that the crossover temperature from the exponential to the saturation regime scales inversely proportional to the MZI arm length. However, the arm length does not vary with the magnetic field in our case. Although we have yet to reach a reasonable explanation, we note that $B \approx 4.3$ T coincides with the field where the characteristic of the edge states changes as we described above (see Fig. 4), which may change the capacitive coupling to the environment.

In addition to the long coherence length, the characteristics of the MZI are significantly stable and reproducible despite several weeks of measurements. The significantly small area enclosed by the two paths (0.02 μm^2 for $w =$

2 nm) prevents the smearing of the interference signal caused by the magnetic field fluctuation. This high stability is a significant difference from the MZIs with the BSs of QPC, which generally requires measurements in short periods [1]. This is an advantage of the proposed scheme for the application of quantum information processing.

III. DISCUSSION AND NUMERICAL SIMULATION

The results mentioned above are summarized as follows: (1) the transition rate of the BSs reached 50%, and (2) the transition is highly coherent, as evidenced by the amplitude of the interference in the MZI. Result (1) presents uncertainty regarding the picture demonstrated in Ref. [30], where the rotation is caused by the abrupt change in the direction of the effective magnetic field, which is the external field plus the SOI field. Because the estimated SOI field $B_{\mathrm{SOI}} \approx 1$ T in the GaAs/(Al, Ga)As heterostructure [51] is smaller than the external magnetic field $B = 4.1$ T, the rotation angle of the effective field at the corner should be less than $\pi/2$. Thus, the spin-flip rate cannot reach 50% in this case.

Instead, the fact that the partition process indicates tunneling between the copropagating edge states at the same Fermi energy should be emphasized. Here, the effective magnetic field presents no energy difference between the initial and final states. On the other hand, tunneling between states with opposite spins requires a variation in the angular momentum. In this case, the only option for the source of angular momentum is the curved orbit around the transition point. The SOI is indispensable for the angular momentum transfer. Furthermore, within the Born approximation [63], the transition matrix for the spin-flip tunneling consists of the SOI terms. Thus, the smaller the turning radius of the BS, the larger the spin-rotation angle owing to the larger local angular momentum.

Numerical simulation.—To examine the aforementioned intuitive inference, the electron transport is numerically studied using the QHECs with the SOI. The schematic of the calculated system is shown in Fig. 7(a). The Hamiltonian is as follows:

$$\mathcal{H} = \frac{\mathbf{\Pi}^2}{2m^*} + V(\mathbf{r}) + H_R + H_D + E_z\sigma^z, \tag{4}$$

where $\mathbf{\Pi} = -i\hbar\nabla + e\mathbf{A}$ is the kinetic momentum, $V(\mathbf{r})$ is the potential forming the waveguide, $H_R = (\alpha/\hbar)\left(\Pi_x\sigma^y - \Pi_y\sigma^x\right)$ and $H_D = (\beta/\hbar)\left(\Pi_x\sigma^x - \Pi_y\sigma^y\right)$ are the Rashba and Dresselhaus type spin-orbit coupling, respectively, and E_z is the Zeeman energy. We adopt the tight-binding approximation and revise the Hamiltonian as follows:

$$\mathcal{H} = \sum_{i,\sigma}\left(V_i + E_z\sigma^z_{\sigma\sigma}\right)c^\dagger_{i\sigma}c_{i\sigma} - \sum_{\langle i,j\rangle,\sigma,\sigma'} h_{i\sigma,j\sigma'}c^\dagger_{i\sigma}c_{j\sigma'}, \tag{5}$$

where $c^\dagger_{i\sigma}(c_{i\sigma})$ is a creation (annihilation) operator of an electron on the site i with spin σ and $\langle i,j\rangle$ indicates the nearest neighbors. The hopping energy $h_{i,j}$ is defined as follows:

$$h_{i,i+\hat{x}} = -V_0 e^{-2\pi i\varphi_i/\varphi_0}\begin{pmatrix} 1 & -\theta_R + i\theta_D \\ -\theta_R + i\theta_D & 1 \end{pmatrix}, \tag{6}$$

$$h_{i,i+\hat{y}} = -V_0\begin{pmatrix} 1 & i\theta_R - \theta_D \\ i\theta_R + \theta_D & 1 \end{pmatrix}, \tag{7}$$

where $V_0 = \hbar^2/2m^*a^2$, a is the lattice constant, φ_0 is the magnetic flux quantum, and $m^* = 0.067m_e$ is the effective mass. $i + \hat{x}$ ($i + \hat{y}$) denotes the nearest neighbor of i along the x (y) axis in the positive direction. The coupling constants of the SOI, α, β are related to θ_R, θ_D by $\alpha = 2\theta_R V_0 a$ and $\beta = 2\theta_D V_0 a$ for small α, β [64]. In the Landau gauge, the magnetic field B is given by $\varphi_i = (y_i - 1)\varphi$, where $\varphi = Ba^2$ is the magnetic flux per lattice cell.

The recursive Green's function method is employed to calculate the electron transport and distribution of the current-carrying state [65,66]. The magnetic flux and Fermi energy of the conduction electron are set to $\varphi = 0.05\varphi_0$ and $E = -3.5V_0$, respectively, to form two QHECs in one of the edges of the system. By choosing the parameters $E_z = 0.15V_0$ and $V_{\mathrm{SF}} = 0.2V_0$, the gate potentials SF_R and SF_L enabled the system to transmit through only one channel. Due to the Zeeman splitting, each electron channel is spin polarized, and the system acted as a spin filter. The system is $200a \times 100a$ in size. An additional gate G_{BS} is introduced to facilitate the beam splitting, which is triangular and characterized by the width W and the height H. The form of the gate potential V_i gradually decreased from the edge of the gates as $V = V_{\mathrm{BS,SF}}\exp(-r/\xi)$, where r is the distance from the edge of the gates and the decay length ξ determines the slope of the potential.

Figures 7(b)–7(d) present the spatial distribution of three different components (σ^z, σ^x, and σ^y) of the current-carrying state for a typical parameter set of $H = 70a$, $W = 25a$, $\xi = 0.5a$, $\theta_R = 0.02\pi$, and $\theta_D = 0.01\pi$. Let us assume $a = 5$ nm to compare the calculated model with the experiments. Then, the area of the system is 1 μm $\times$ 0.5 μm, and the other parameters are as follows: $V_0 = 23$ meV, $B = 4.1$ T, $g^* = E_z/\mu_B B = 14$, $\alpha = 1.4 \times 10^{-11}$ eVm, and $\beta = 7.1 \times 10^{-12}$ eVm. Note, these parameters are tuned to clarify the essential legitimacy of our hypothesis and are not necessarily the same as those in the experiment. Namely, the simulation does not include several significant factors, such as the Coulomb interaction and, thus, cannot be directly compared. Instead, the qualitative and half-quantitative (relationship between the amplitudes of the effective magnetic fields and the spin-rotation angle) properties should be emphasized.

Figure 7(b) demonstrates that the gate SF_R functions as a spin filter, and only the up-spin current goes through the

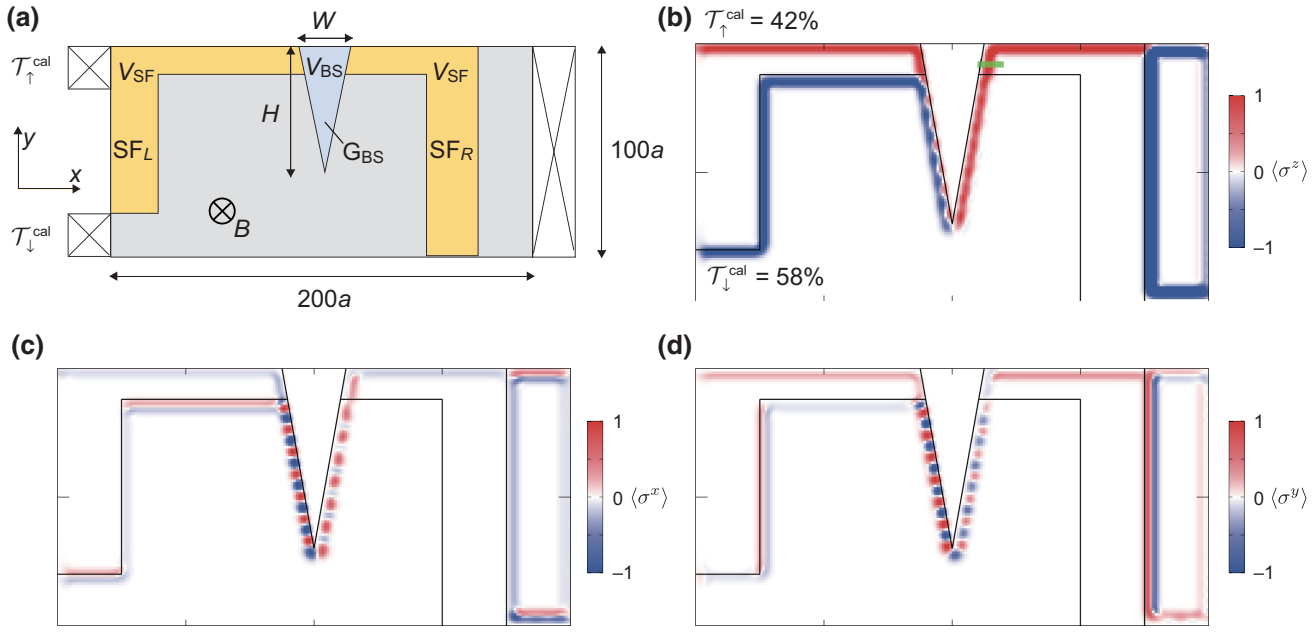

FIG. 7. (a) Schematic of the model used for the simulation of the BS. Spin-filter gates SF_R and SF_L correspond to SF_b and SF_c in the experiment, respectively. The potential is set to V_{SF} in the yellow regions. The blue-gray triangular gate G_{BS} with potential V_{BS} corresponds to gate G_a in the experiment. Outgoing normal leads are attached to the left side of the sample. (b) Calculated distribution of the σ^z component $\langle\sigma^z\rangle$ of the current carrying state, (c) σ^x component $\langle\sigma^x\rangle$, and (d) σ^y component $\langle\sigma^y\rangle$.

gate. The clear spin-flip interchannel transition is observed at the bottom corner of the gate G_{BS}, validating our interpretation of the experimental results. The calculated transition probability is $\mathcal{T}_\downarrow^{\rm cal} = 58\%$ for this parameter set. Note, the ratio of the SOI field to the external field B_{SOI}/B in this simulation is estimated to be 0.26 by assuming $B_{SOI}/B \approx \left\langle \sqrt{\sigma_x^2 + \sigma_y^2}/\sigma_z \right\rangle$, where the expectation value is obtained along the green line denoted in Fig. 7(b). Thus, despite the condition where B_{SOI} is smaller than B, the transition probability reaches 50%, supporting our intuitive discussion. After the transition, the spin-up and spin-down wave functions copropagate along the left side of the gate G_{BS}, demonstrating a periodic change in the $\langle\sigma^z\rangle$, which is also observed in the $\langle\sigma^x\rangle$ and $\langle\sigma^y\rangle$ components shown in Figs. 7(c) and 7(d), representing the spin precession. The small spin-flip interchannel transition occurs when the current leaves and re-enters the spin-filter gate, leading to an AB oscillation, which explains the small oscillation in $\mathcal{T}_\downarrow$ observed in the experiment, as shown in Figs. 2(a) and 2(b) below $V_a \approx -0.9$ V.

Figure 8(a) demonstrates $\mathcal{T}_\downarrow^{\rm cal}$ as a function of the height of the triangular gate potential H, with a fixed width of $W = 25a$. $\mathcal{T}_\downarrow^{\rm cal}$ is apparently enhanced by increasing H. Therefore, the sharp angle of the vertex of the triangular gate potential can be concluded to enhance the spin-flip interchannel transition. We obtain a half-mirror ($\mathcal{T}_\downarrow = 50\%$) for $H \cong 65a$.

The experimental results in Fig. 2 demonstrate that $\mathcal{T}_\downarrow^{\rm cal}$ increases by applying a larger negative gate voltage. This situation can be modeled by changing the decay length ξ of the gate-defined potential. Figure 8(b) demonstrates $\mathcal{T}_\downarrow^{\rm cal}$ as a function of ξ. $\mathcal{T}_\downarrow^{\rm cal}$ increases as ξ decreases, with a slight oscillatory variation. The reason for the increasing $\mathcal{T}_\downarrow^{\rm cal}$ is as follows. First, the larger the potential gradient (smaller ξ) at the position of the edge channel, the smaller the distance between the gate edge to the edge channels, leading to the larger curvature of the corner. This enhances the nonadiabaticity of the transition. Second, as the potential gradient becomes larger, the width of the potential barrier between the spin-split edge channels becomes narrower, leading to an enhanced tunneling probability. The oscillatory variation is most likely caused by the phase modulation of the AB interference when the potential gradient at the edge channels is varied.

Figure 8(c) demonstrates $\mathcal{T}_\downarrow^{\rm cal}$ as a function of θ_R with $\theta_D = 0.01\pi$. $\mathcal{T}_\downarrow^{\rm cal}$ increases from $\theta_R = 0$ to 0.02π, and oscillates for a larger θ_R, which is sufficiently explained by the Rabi oscillation caused by the rotating effective field B_{SOI} at the corner of the BS. Note, when the Hamiltonian does not contain the spin-orbit term ($\theta_R = \theta_D = 0$), which is not shown in the figure, $\mathcal{T}_\downarrow$ becomes zero, indicating that the SOI is indispensable for the interchannel transition.

To summarize the simulation, the numerical simulation based on the recursive Green's function method successfully reproduces the experimental results, not only qualitatively but half-quantitatively, particularly in the zenith angle rotation of spin. The result strongly supports

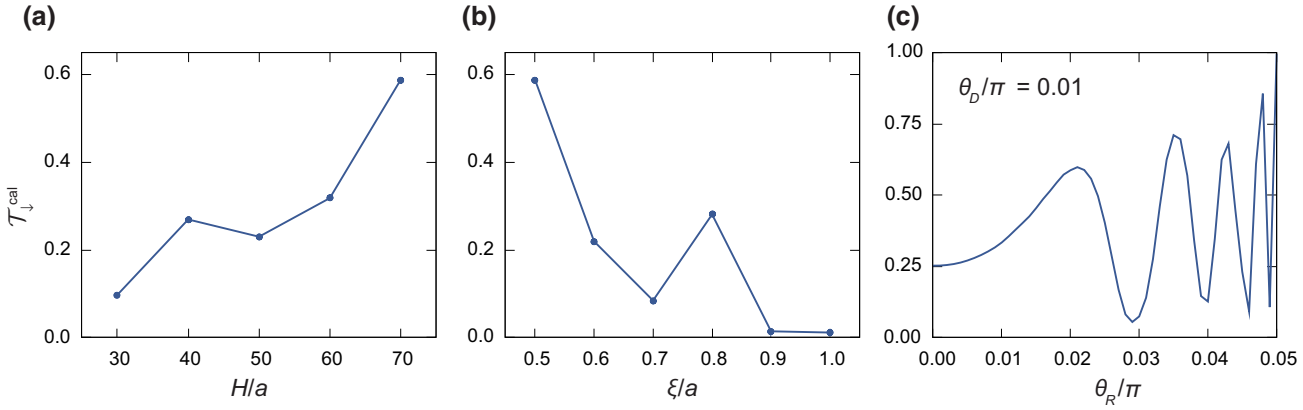

FIG. 8. Calculated transition probability $\mathcal{T}_{\downarrow}^{cal}$ as a function of three different parameters. (a) $\mathcal{T}_{\downarrow}^{cal}$ as a function of the height H of the triangular gate potential, with a fixed width of $W = 25a$. The strength of SOI is set to $\theta_R = 0.02\pi$ and $\theta_D = 0.01\pi$. $\xi = 0.5a$. (b) $\mathcal{T}_{\downarrow}^{cal}$ as a function of the decay length of the potential ξ. Other parameters are as follows: $H = 70a$, $W = 25a$, $\theta_R = 0.02\pi$, $\theta_D = 0.01\pi$. (c) $\mathcal{T}_{\downarrow}^{cal}$ as a function of the strength of the Rashba SOI θ_R. Other parameters are as follows: $H = 70a$, $W = 25a$, $\theta_D = 0.01\pi$, and $\xi = 0.5a$.

our inference regarding the spin-rotation mechanism of the SOI-aided interchannel quantum tunneling.

IV. CONCLUDING REMARK

We investigate the BS on copropagating QHECs using a metal gate with an acute angle corner. The interchannel transitions accompanied by spin flips are caused by SOIs and the orbital angular momentum created at the sharp corner of the QHECs. The transition probability of the BS can be controlled from approximately 0% to over 50% by modulating the distance of the copropagating QHECs via the gate voltage. We compose a MZI with the BSs, demonstrating a high visibility in the interference pattern of up to 85%, indicating a high quantum coherence in the transition over the BS. We deduce the coherence length from the temperature dependence of the visibility. The long coherence length exceeding 200 μm highlights the robustness of the copropagating (Equi-Landau-level) channels against the external source of the decoherence. The device characteristics are very stable, reflecting its compactness. The results present a convenient, stable, and scalable way of processing quantum information in the flying qubit scheme.

ACKNOWLEDGMENTS

We thank Dr Hashisaka Masayuki for the fruitful discussion. A suggestion on the coherence length from a referee is constructive. This work is partly supported by JSPS KAKENHI Grants No. JP19H00652, No. 19K05253, No. 21H05016, and No. 21H01799.

[1] Y. Ji, Y. Chung, D. Sprinzak, M. Heiblum, D. Mahalu, and H. Shtrikman, An electronic Mach-Zehnder interferometer, Nature **422**, 415 (2003).

[2] J. Nakamura, S. Fallahi, H. Sahasrabudhe, R. Rahman, S. Liang, G. C. Gardner, and M. J. Manfra, Aharonov–Bohm interference of fractional quantum Hall edge modes, Nat. Phys. **15**, 563 (2019).

[3] J. Nakamura, S. Liang, G. C. Gardner, and M. J. Manfra, Direct observation of anyonic braiding statistics, Nat. Phys. **16**, 931 (2020).

[4] E. Bocquillon, F. D. Parmentier, C. Grenier, J.-M. Berroir, P. Degiovanni, D. C. Glattli, B. Plaçais, A. Cavanna, Y. Jin, and G. Fève, Electron Quantum Optics: Partitioning Electrons One by One, Phys. Rev. Lett. **108**, 196803 (2012).

[5] M. Yamamoto, S. Takada, C. Bäuerle, K. Watanabe, A. D. Wieck, and S. Tarucha, Electrical control of a solid-state flying qubit, Nat. Nanotechnol. **7**, 247 (2012).

[6] A. Bertoni, P. Bordone, R. Brunetti, C. Jacoboni, and S. Reggiani, Quantum Logic Gates based on Coherent Electron Transport in Quantum Wires, Phys. Rev. Lett. **84**, 5912 (2000).

[7] C. Bauerle, D. C. Glattli, T. Meunier, F. Portier, P. Roche, P. Roulleau, S. Takada, and X. Waintal, Coherent control of single electrons: a review of current progress, Rep. Prog. Phys. **81**, 056503 (2018).

[8] H. Edlbauer *et al.*, Semiconductor-based electron flying qubits: review on recent progress accelerated by numerical modelling, EPJ Quantum Technol. **9**, 21 (2022).

[9] G. Fève, A. Mahé, J.-M. Berroir, T. Kontos, B. Plaçais, D. C. Glattli, A. Cavanna, B. Etienne, and Y. Jin, An on-demand coherent single-electron source, Science **316**, 1169 (2007).

[10] S. P. Giblin, M. Kataoka, J. D. Fletcher, P. See, T. J. B. M. Janssen, J. P. Griffiths, G. A. C. Jones, I. Farrer, and D. A.

Ritchie, Towards a quantum representation of the ampere using single electron pumps, Nat. Commun. **3**, 930 (2012).
[11] M. Kataoka, N. Johnson, C. Emary, P. See, J. P. Griffiths, G. A. C. Jones, I. Farrer, D. A. Ritchie, M. Pepper, and T. J. B. M. Janssen, Time-of-Flight Measurements of Single-Electron Wave Packets in Quantum Hall Edge States, Phys. Rev. Lett. **116**, 126803 (2016).
[12] N. Ubbelohde, F. Hohls, V. Kashcheyevs, T. Wagner, L. Fricke, B. Kaestner, K. Pierz, H. W. Schumacher, and R. J. Haug, Partitioning of on-demand electron pairs, Nat. Nanotechnol. **10**, 46 (2015).
[13] L. Freise, T. Gerster, D. Reifert, T. Weimann, K. Pierz, F. Hohls, and N. Ubbelohde, Trapping and Counting Ballistic Nonequilibrium Electrons, Phys. Rev. Lett. **124**, 127701 (2020).
[14] L. Bellentani, G. Forghieri, P. Bordone, and A. Bertoni, Two-electron selective coupling in an edge-state based conditional phase shifter, Phys. Rev. B **102**, 035417 (2020).
[15] S. Hermelin, S. Takada, M. Yamamoto, S. Tarucha, A. D. Wieck, L. Saminadayar, C. Bäuerle, and T. Meunier, Electrons surfing on a sound wave as a platform for quantum optics with flying electrons, Nature **477**, 435 (2011).
[16] H. Sanada, Y. Kunihashi, H. Gotoh, K. Onomitsu, M. Kohda, J. Nitta, P. V. Santos, and T. Sogawa, Manipulation of mobile spin coherence using magnetic-field-free electron spin resonance, Nat. Phys. **9**, 280 (2013).
[17] Y. Yamamoto, C. Santori, G. Solomon, J. Vuckovic, D. Fattal, E. Waks, and E. Diamanti, Single photons for quantum information systems, Prog. Inf. **1**, 5 (2005).
[18] B. J. van Wees, H. van Houten, C. W. J. Beenakker, J. G. Williamson, L. P. Kouwenhoven, D. van der Marel, and C. T. Foxon, Quantized Conductance of Point Contacts in a Two-Dimensional Electron Gas, Phys. Rev. Lett. **60**, 848 (1988).
[19] M. Büttiker, Absence of backscattering in the quantum Hall effect in multiprobe conductors, Phys. Rev. B **38**, 9375 (1988).
[20] D. P. DiVincenzo, The Physical Implementation of Quantum Computation, Fortschritte der Phys. **48**, 771 (2000).
[21] R. Ionicioiu, G. Amaratunga, and F. Udrea, Quantum computation with ballistic electrons, Int. J. Mod. Phys. B **15**, 125 (2001).
[22] D. J. Reilly, C. M. Marcus, M. P. Hanson, and A. C. Gossard, Fast single-charge sensing with a rf quantum point contact, Appl. Phys. Lett. **91**, 162101 (2007).
[23] V. Giovannetti, F. Taddei, D. Frustaglia, and R. Fazio, Multichannel architecture for electronic quantum Hall interferometry, Phys. Rev. B **77**, 155320 (2008).
[24] E. V. Deviatov, S. V. Egorov, G. Biasiol, and L. Sorba, Quantum Hall Mach-Zehnder interferometer at fractional filling factors, EPL (Europhys. Lett.) **100**, 67009 (2012).
[25] E. V. Deviatov and A. Lorke, Experimental realization of a Fabry-Perot-type interferometer by copropagating edge states in the quantum Hall regime, Phys. Rev. B **77**, 161302(R) (2008).
[26] E. V. Deviatov, A. Ganczarczyk, A. Lorke, G. Biasiol, and L. Sorba, Quantum Hall Mach-Zehnder interferometer far beyond equilibrium, Phys. Rev. B **84**, 235313 (2011).
[27] B. Karmakar, D. Venturelli, L. Chirolli, F. Taddei, V. Giovannetti, R. Fazio, S. Roddaro, G. Biasiol, L. Sorba, V. Pellegrini, and F. Beltram, Controlled Coupling of Spin-Resolved Quantum Hall Edge States, Phys. Rev. Lett. **107**, 236804 (2011).
[28] B. Karmakar, D. Venturelli, L. Chirolli, V. Giovannetti, R. Fazio, S. Roddaro, L. N. Pfeiffer, K. W. West, F. Taddei, and V. Pellegrini, Nanoscale Mach-Zehnder interferometer with spin-resolved quantum Hall edge states, Phys. Rev. B **92**, 195303 (2015).
[29] T. Nakajima, K.-T. Lin, and S. Komiyama, Gate-control of spin precession in quantum Hall edge states, (2012), arXiv preprint ArXiv:1207.7243.
[30] T. Nakajima, K. T. Lin, and S. Komiyama, Electrical control of flying spin precession in chiral 1D edge states, AIP Conf. Proc. **1566**, 301 (2013).
[31] S. M. Frolov, S. Luscher, W. Yu, Y. Ren, J. A. Folk, and W. Wegscheider, Ballistic spin resonance, Nature **458**, 868 (2009).
[32] T. Shimizu, T. Nakamura, Y. Hashimoto, A. Endo, and S. Katsumoto, Gate-controlled unitary operation on flying spin qubits in quantum Hall edge states, Phys. Rev. B **102**, 235302 (2020).
[33] J. J. Palacios and C. Tejedor, Effects of geometry on edge states in magnetic fields: Adiabatic and nonadiabatic behavior, Phys. Rev. B **45**, 9059 (1992).
[34] L. Bellentani, A. Beggi, P. Bordone, and A. Bertoni, Dynamics and Hall-edge-state mixing of localized electrons in a two-channel Mach-Zehnder interferometer, Phys. Rev. B **97**, 205419 (2018).
[35] M. Hashisaka, N. Hiyama, T. Akiho, K. Muraki, and T. Fujisawa, Waveform measurement of charge- and spin-density wavepackets in a chiral Tomonaga–Luttinger liquid, Nat. Phys. **13**, 559 (2017).
[36] M. Hashisaka and T. Fujisawa, Tomonaga-Luttinger-liquid nature of edge excitations in integer quantum Hall edge channels, Rev. Phys. **3**, 32 (2018).
[37] Y. Kunihashi, H. Sanada, H. Gotoh, K. Onomitsu, M. Kohda, J. Nitta, and T. Sogawa, Drift transport of helical spin coherence with tailored spin–orbit interactions, Nat. Commun. **7**, 10722 (2016).
[38] See Supplemental Material at http://link.aps.org/supplemental/10.1103/PhysRevApplied.19.034085 for more information on the quantum Hall characteristics, conductance versus the spin-filter voltages at several external magnetic fields, electrostatic potential simulation using the density-gradient theory, effects of the inner-edge channels in the $\nu = 4$ quantum Hall edge state, effects of the spin-filter voltages on the interference in the BS, and measurement results of the "Control device".
[39] D. B. Chklovskii, B. I. Shklovskii, and L. I. Glazman, Electrostatics of edge channels, Phys. Rev. B **46**, 4026 (1992).
[40] I. A. Larkin and J. H. Davies, Edge of the two-dimensional electron gas in a gated heterostructure, Phys. Rev. B **52**, R5535 (1995).
[41] I. Strzalkowski, S. Joshi, and C. R. Crowell, Dielectric constant and its temperature dependence for GaAs, CdTe, and ZnSe, Appl. Phys. Lett. **28**, 350 (1976).
[42] S. Ihnatsenka and I. V. Zozoulenko, Spin polarization of edge states and the magnetosubband structure in quantum wires, Phys. Rev. B **73**, 075331 (2006).

[43] S. Ihnatsenka and I. V. Zozoulenko, Spatial spin polarization and suppression of compressible edge channels in the integer quantum Hall regime, Phys. Rev. B **73**, 155314 (2006).
[44] S. Ihnatsenka and I. V. Zozoulenko, Magnetoconductance of interacting electrons in quantum wires: Spin density functional theory study, Phys. Rev. B **78**, 035340 (2008).
[45] T. Nakajima, Y. Kobayashi, and S. Komiyama, Spin-textured edge states probed by local nuclear spin polarization, Phys. Rev. B **82**, 201302(R) (2010).
[46] A. Karlhede, S. A. Kivelson, K. Lejnell, and S. L. Sondhi, Textured Edges in Quantum Hall Systems, Phys. Rev. Lett. **77**, 2061 (1996).
[47] M. Franco and L. Brey, Phase diagram of a quantum Hall ferromagnet edge, spin-textured edges, and collective excitations, Phys. Rev. B **56**, 10383 (1997).
[48] J. Sjöstrand, A. Eklund, and A. Karlhede, $\nu = 1$ quantum Hall edge with a realistic potential, Phys. Rev. B **66**, 165308 (2002).
[49] T. Ando and Y. Uemura, Theory of oscillatory g factor in an MOS inversion layer under strong magnetic fields, J. Phys. Soc. Jpn. **37**, 1044 (1974).
[50] A. Endo, K. Koike, S. Katsumoto, and Y. Iye, Frequencies of the edge-magnetoplasmon excitations in gated quantum Hall edges, J. Phys. Soc. Jpn. **87**, 064709 (2018).
[51] G. Müller, D. Weiss, A. V. Khaetskii, K. von Klitzing, S. Koch, H. Nickel, W. Schlapp, and R. Lösch, Equilibration length of electrons in spin-polarized edge channels, Phys. Rev. B **45**, 3932 (1992).
[52] A. V. Khaetskii, Transitions between spin-split edge channels in the quantum-Hall-effect regime, Phys. Rev. B **45**, 13777 (1992).
[53] D. G. Polyakov, Spin-flip scattering in the quantum Hall regime, Phys. Rev. B **53**, 15777 (1996).
[54] P. Roulleau, F. Portier, P. Roche, A. Cavanna, G. Faini, U. Gennser, and D. Mailly, Direct Measurement of the Coherence Length of Edge States in the Integer Quantum Hall Regime, Phys. Rev. Lett. **100**, 126802 (2008).
[55] L. V. Litvin, A. Helzel, H.-P. Tranitz, W. Wegscheider, and C. Strunk, Edge-channel interference controlled by landau level filling, Phys. Rev. B **78**, 075303 (2008).
[56] P. Roulleau, F. Portier, P. Roche, A. Cavanna, G. Faini, U. Gennser, and D. Mailly, Noise Dephasing in Edge States of the Integer Quantum Hall Regime, Phys. Rev. Lett. **101**, 186803 (2008).
[57] H. Duprez, E. Sivre, A. Anthore, A. Aassime, A. Cavanna, A. Ouerghi, U. Gennser, and F. Pierre, Macroscopic Electron Quantum Coherence in a Solid-State Circuit, Phys. Rev. X **9**, 021030 (2019).
[58] P.-A. Huynh, F. Portier, H. le Sueur, G. Faini, U. Gennser, D. Mailly, F. Pierre, W. Wegscheider, and P. Roche, Quantum Coherence Engineering in the Integer Quantum Hall Regime, Phys. Rev. Lett. **108**, 256802 (2012).
[59] E. Buks, R. Schuster, M. Heiblum, D. Mahalu, and V. Umansky, Dephasing in electron interference by a 'which-path' detector, Nature **391**, 871 (1998).
[60] M. Jo, J.-Y. M. Lee, A. Assouline, P. Brasseur, K. Watanabe, T. Taniguchi, P. Roche, D. C. Glattli, N. Kumada, F. D. Parmentier, H.-S. Sim, and P. Roulleau, Scaling behavior of electron decoherence in a graphene Mach-Zehnder interferometer, Nat. Commun. **13**, 5473 (2022).
[61] M. Jo, P. Brasseur, A. Assouline, G. Fleury, H.-S. Sim, K. Watanabe, T. Taniguchi, W. Dumnernpanich, P. Roche, D. C. Glattli, N. Kumada, F. D. Parmentier, and P. Roulleau, Quantum Hall Valley Splitters and a Tunable Mach-Zehnder Interferometer in Graphene, Phys. Rev. Lett. **126**, 146803 (2021).
[62] M. Hashisaka, A. Helzel, S. Nakamura, L. Litvin, Y. Yamauchi, K. Kobayashi, T. Ono, H.-P. Tranitz, W. Wegscheider, and C. Strunk, Temperature dependence of the visibility in an electronic Mach-Zehnder interferometer, Phys. E: Low-Dimens. Syst. Nanostruct. **42**, 1091 (2010).
[63] L. Chirolli, D. Venturelli, F. Taddei, R. Fazio, and V. Giovannetti, Proposal for a Datta-Das transistor in the quantum Hall regime, Phys. Rev. B **85**, 155317 (2012).
[64] J.-i. Ohe, M. Yamamoto, T. Ohtsuki, and J. Nitta, Mesoscopic Stern-Gerlach spin filter by nonuniform spin-orbit interaction, Phys. Rev. B **72**, 041308(R) (2005).
[65] P. A. Lee and D. S. Fisher, Anderson Localization in Two Dimensions, Phys. Rev. Lett. **47**, 882 (1981).
[66] T. Ando, Quantum point contacts in magnetic fields, Phys. Rev. B **44**, 8017 (1991).